Optics Letters

Two-photon PSF-engineered image scanning microscopy

Omer Tzang,[1] Dan Feldkhun,[1] Anurag Agrawal,[2] Alexander Jesacher,[3,*] and Rafael Piestun[1]

[1]Department of Electrical and Computer Engineering, University of Colorado, Boulder, Colorado 80309, USA
[2]Double Helix Optics, Boulder, Colorado 80309, USA
[3]Division of Biomedical Physics, Medical University of Innsbruck, Müllerstraße 44, 6020 Innsbruck, Austria
*Corresponding author: alexander.jesacher@i-med.ac.at

Received 13 November 2018; accepted 11 December 2018; posted 20 December 2018 (Doc. ID 351579); published 7 February 2019

We present two-photon fluorescence image scanning microscopy (ISM) with engineered excitation and detection point-spread-functions enabling 3D imaging in a single 2D scan. This demonstration combines excitation using a holographic multispot array of focused femtosecond pulses with a high-efficiency single-helix PSF phase mask detection. Camera detection along with a multiview reconstruction algorithm allows volumetric imaging of biological samples over a depth of field spanning more than 1500 nm with an axial resolution of better than 400 nm. The nonlinear two-photon process improves sectioning and the inherent longer wavelengths increase the penetration depth in scattering samples. Our method extends the performance of 3D ISM towards thicker biological samples.

https://doi.org/10.1364/OL.44.000895

Laser scanning microscopes are helpful tools for the visualization of 3D structures at the submicron scale. By pointwise raster scanning the sample with a tightly focused laser spot, they collect sample information in a sequential manner. Two-photon excitation scanning fluorescence microscopy [1] is a powerful method for imaging deep into scattering tissues [2]. Near infra-red excitation wavelengths and short pulses are typically used to generate fluorescence emission of labeled samples through nonlinear two-photon excitation. The near-infrared wavelengths scatter less than visible light and enable deeper penetration into biological tissue [3]. The nonlinear signal generation ensures that the signal is predominantly generated in the focal spot and improves z-sectioning capabilities by suppression of an out-of-focus background.

While for highly scattering samples such as brain tissue and penetration depths exceeding several hundred microns or more, it may not be feasible to directly image the focal plane onto a camera; it is possible for moderately scattering tissues and/or smaller imaging depths. In such situations, reimaging the fluorescence signal like in a confocal microscope allows one to obtain even higher resolution by implementing the concept of ISM [4–7].

ISM is a powerful scanning microscopy method that can achieve the theoretical maximum resolution of a confocal microscope at a very high collection efficiency [8,9]. The origin of its high-level performance is the use of point-scanning in conjunction with a pixelated detector, where each pixel acts as an individual confocal bucket detector collecting an individual high-resolution image of the sample. Because many pixels are used and practically no light is discarded by a pinhole such as in a traditional confocal, the method is very light efficient. Data postprocessing in the form of pixel-reassignment [8] or multiview image fusion [10,11] finally enables the construction of a bright high-resolution image from these multiple views.

Previous publications highlighted the advantages of combining PSF-engineering with ISM [11–13], which we refer to as *engineered Image Scanning Microscopy (eISM)* [13]. By specifically tailoring the microscope's PSF, the information collected by the detector is diversified (i.e., every camera pixel detects a different z plane or color) and enables the retrieval of additional sample properties, which otherwise would require additional scans with different system settings. Examples for such additional information are 3D structural [12,13] or spectroscopic information [14].

In this Letter, we report, to our knowledge, the first combination of eISM with two-photon excitation, which we further denote as 2ph-eISM. We use a 3D-encoding PSF, which enables the acquisition of 3D structural information in a single 2D scan. A related configuration was recently demonstrated for linear fluorescence [11,13]. 2ph-eISM combines the advantages of nonlinear imaging with eISM.

Figure 1 shows a sketch of the experimental setup. A tunable femtosecond laser (Coherent Chameleon) is wavefront-shaped by a liquid crystal SLM (Meadowlark 512L PCIe) and coupled into a side port of a commercial epi-detection microscope (Zeiss Observer.Z1) equipped with a 1.3 NA objective (Zeiss Plan-Neofluar 100×). The SLM and the objective pupil are in conjugate planes. Calculated holograms [15] displayed on the SLM generate multispot arrays where each spot is focused on a selected z plane. Raster-scanning of specimens is performed with a piezostage (PI P-733.3). The generated two-photon fluorescence is filtered by a dichroic mirror and a short-pass emission filter and spatially filtered by a single-helix phase mask [16],

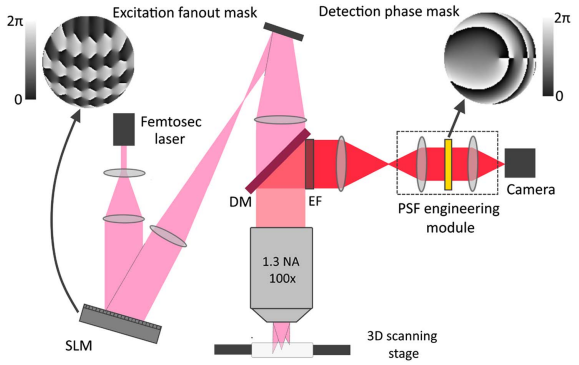

Fig. 1. Optical setup for 2ph-eISM. A NIR beam from a fs-laser is expanded and reflected off a LCoS SLM. A calculated phase hologram (shown in the top left inset) generates multiple spots in the focal space. Fluorescence emission at visible wavelengths is filtered by a dichroic mirror (DM) followed by a bandpass emission filter (EF). PSF engineering on the detection side is performed by a single-helix phase mask (shown in the top right inset) mounted in a PSF engineering commercial module (Double Helix, SPINDLE) attached to a camera port. A 3D piezo stage is used for scanning.

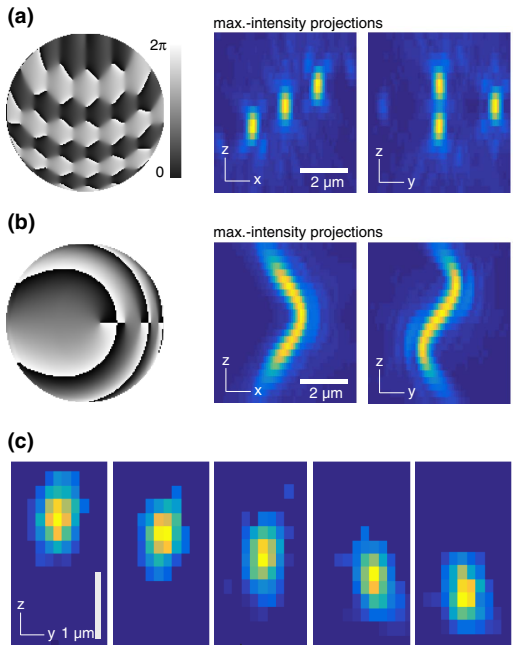

Fig. 2. Illumination, collection, and system PSFs of 2ph-eISM. (a) and (b) Excitation and detection phase masks (left), and simulated maximum-intensity projections of the corresponding PSFs (right). (c) Sections through five exemplary total PSFs. Their different z locations are clearly visible. Sections through all 50 measured engineered PSFs and those of regular 2ph-ISM are shown in Visualization 1 and Visualization 2, respectively.

mounted in a plane conjugate to the objective pupil that is made accessible by a PSF engineering module (Double Helix SPINDLE). The PSF shaped by the single-helix phase mask stretches considerably more along the optical axis than an unmodified Gaussian PSF [11,17,18]. It also provides higher efficiency compared to liquid crystal SLM-based wavefront shaping, because the phase mask presents no dependence on the light polarization. The detection is performed by a sCMOS camera (Hamamatsu ORCA-Flash 4.0), which takes images of small regions around every scan point.

Details of the PSF engineering are outlined in Fig. 2. The excitation phase mask (shown at the top left) generates three foci along a spiral around the focal region, with lateral and axial interspacings of 2 and 0.7 µm, respectively. The programmed (x, y, z) spot positions (in units of µm) are: (–1, 0, 0.7), (0, 1.73, 0), and (1, 0, –0.7). The calculated diffraction efficiency of the excitation phase hologram is 85%. In practice, the efficiency is somewhat lower due to SLM limitations. On the emission side, the helical phase mask shapes the detection PSF into a single-helix with a high efficiency of more than 90%. Maximum-intensity projections of the simulated excitation and detection PSFs are shown at the right of the figure.

It is important to emphasize that the total PSFs describing the image formation for each detector pixel look strikingly different from both the excitation and detection PSFs. They are the product of the excitation PSF and a correctly shifted detection PSF [13], and are of an approximate 3D Gaussian shape. Compared to the PSFs of regular 2ph-ISM [4–6], however, they cover varying axial positions within a depth of several wavelengths, which ultimately enables the collection of 3D information. Sections through five measured representative total PSFs are shown in Fig. 2(c). Sections through all 50 engineered PSFs used for data reconstruction are provided in the supplemental material.

Figure 3 quantifies experimentally determined imaging properties of 2ph-eISM and regular 2ph-ISM, respectively, from 3D scans over fluorescent beads (Tetraspeck, 200 nm diameter).

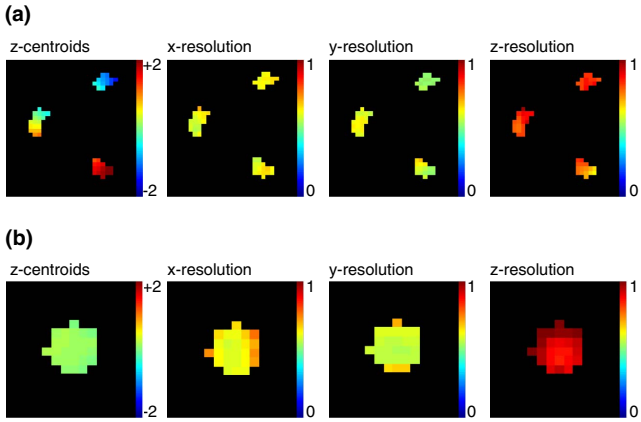

Fig. 3. (a) Measured z positions and widths of the PSFs of 2ph-eISM and (b) regular 2ph-ISM. All values are in units of the main emission wavelength in a medium with refractive index 1.52 (λ_{em} = 430 nm). Each image represents the central region of the camera sensor. The colored camera pixels are those used for data reconstruction, i.e., each of them corresponds to an individual confocal image. The colors encode the z centroid as well as x, y, and z widths (FWHM) of 3D Gaussian fits to the respective PSFs. The spatial resolutions of both methods are comparable.

The figure contains eight square images, each representing the central camera region. To restrict the data volume, only the colored pixels are used for data reconstruction. The 25 pixels used for regular 2ph-ISM contain about two thirds of the signal

energy reaching the shown central camera region, and the 50 pixels used for 2ph-eISM contain about one third of the signal energy. In each image of the central camera region, the color of a particular pixel reflects a specific property of the corresponding PSF, such as its axial position (z centroid) and FWHM-values along the x, y, and z directions of a 3D Gaussian fit to the PSF.

When comparing the modified imaging system with regular 2ph-ISM, it is apparent that the PSFs of the former are evenly distributed within an axial range of about 3.5 emission wavelengths (λ_{em}), which equals about four axial planes when taking the z resolution of 0.8 λ_{em} into account. The z resolution can be inferred from the last image in Fig. 3(a). Conversely, the PSFs of regular 2ph-ISM are all located in a single common z plane. On the other hand, Fig. 3 shows that the x, y, and z resolutions of 2ph-eISM (a) and 2ph-ISM (b) are comparable.

It is also interesting to compare the two photon ISM resolution to that obtained with linear ISM, which has for instance been investigated in Ref. [13]. Here, the main difference applies to the z resolution, which is below 1 λ_{em} for all 25 detector pixels in the two-photon case, whereas for linear fluorescence the z resolutions of off-axis pixels are significantly worse than that of the best-performing on-axis pixel (up to about 2 λ_{em}).

To highlight the advantage of two-photon imaging over linear fluorescence, we first compare regular ISM and 2ph-ISM images at a single confocal plane. Figure 4 shows experimental images of a multiply stained rat kidney tissue section. We compare a linear florescence scan (using a 670 nm CW laser and appropriate filters) with a 2ph-ISM image of the same area. The suppression of the out-of-focus background in the two-photon image, depicted in Fig. 4(b) leads to significantly better optical sectioning. The images shown in this comparison have been pixel-reassigned as described in Ref. [19], but not deconvolved.

Next, the 3D imaging capabilities of the 2ph-eISM implementation are demonstrated. Figure 5 shows the result of a single scan over an area of 28 × 28 μm on our stained-cell sample, after 3D image reconstruction using 100 iterations. Image reconstruction is performed by combining the information contained in the single-detector 2ph-eISM images of 50 detector pixels using multiview Richardson–Lucy deconvolution [11,13]. The scan step-size was 100 nm, and the acquisition time per scan point was 50 ms. Therefore, the total exposure time is about 1 h. The fs-laser was tuned to 740 nm to maximize the excitation of the fluorophore. The three larger images on the left of the figure show sample sections located at −400, 0, and +400 nm and the unique cellular features in each of them. The image series on the right shows the square region marked in the middle large image at seven different axial planes, separated by regular interspacings of 200 nm. Remarkably, the entire information shown in the figure was acquired in a single 2D scan.

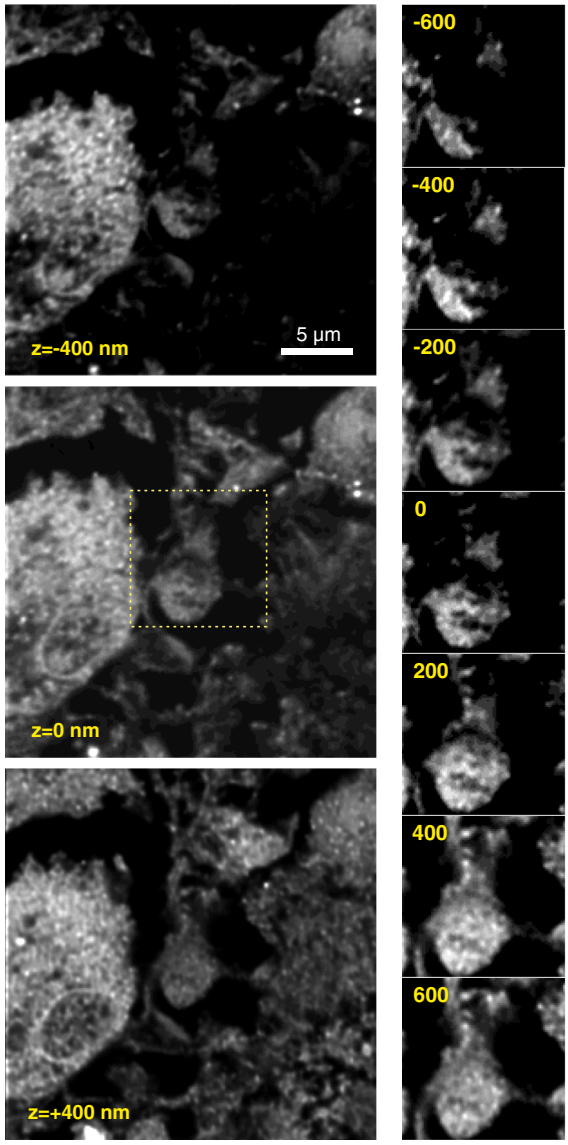

Fig. 5. Experimental 2ph-eISM volume image of a kidney tissue section. Three selected larger sections are shown on the left. The image planes are located at relative axial positions of −400, 0, and +400 nm, respectively. The region marked in the middle large image is shown at seven different axial planes on the right column.

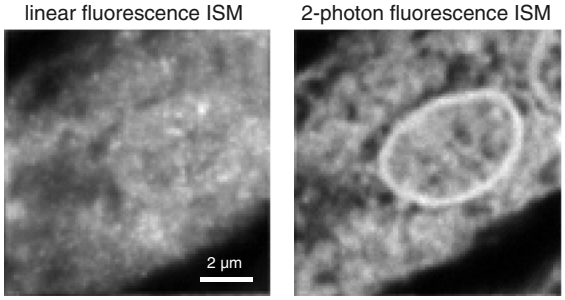

Fig. 4. Comparison of linear and 2ph-ISM. The sample is a multiply stained rat kidney tissue section. No phase engineering is used in either case. (a) Linear fluorescence image using a 670 nm CW laser excitation. (b) Two-photon fluorescence image using 740 nm fs-laser excitation after pixel reassignment.

We presented phase-engineered two-photon excitation fluorescence ISM. The PSFs of each pixel in the detector array were tailored to collect sample information from an extended axial range, thus enabling 3D imaging in a single planar scan. The implemented phase engineering method combines beam splitting in the excitation path with single-helix PSF detection, facilitating signal detection over an axial range spanning 3.5 λ_{em} in the configuration shown.

The spatial resolution of the method is practically equal to that of regular 2ph-ISM. For both cases, we measured $x - y$

resolutions of about 260 nm (equals 0.6 λ_{em}) and z resolutions of about 360 nm (0.8 λ_{em}), respectively.

The upper limits for imaging speeds achievable with our method depend on the hardware used and scan strategy, predominantly on the type of detector used (multichannel PMT/APD or camera) and whether a single- or multispot excitation is pursued. From a more fundamental point of view, it depends on the amount of information that is collectable in a given time-frame and how well this information capacity can be utilized. Modern sCMOS cameras, for instance, support multirow readout (e.g., eight rows, 2048 columns) at approximately 25 kHz, corresponding to about 400 Mpix/s. However, accessing this capacity demands a multispot excitation scheme, which requires keeping enough distance between the spots. Therefore, a significant fraction of these pixels is *empty*, thus reducing the information collection rate. On the other hand, a 32-channel PMT or APD offers sufficient detectors to capture the entire 3D information from a single scan spot. If combined with a fast scanning scheme, such as a resonant or acoustic scanner, the volume acquisition rate can be 30 Hz or more.

The fluorescence emission from stained biological samples is often an unpolarized low-SNR signal, and its detection can be challenging. Therefore, any mask at the detection side used for PSF engineering should be designed for high diffraction efficiency and transmission. We used a lithographically fabricated phase mask with efficiency of more than 90% for both polarizations that dramatically improves the detection efficiency relative to using a liquid crystal SLM.

We believe that a 3D-mode of 2ph-eISM such as presented here can lead to an acquisition speed improvement in volumetric imaging, predominantly for scenarios where the z range of interest is already covered by the axial detection range, thus avoiding the mechanical z stepping.

In conclusion, we presented a two-photon scanning microscope that is capable of recording 3D information from a single planar scan of weakly scattering samples. This was achieved by combining image-based multispot parallel scanning with NIR wavelengths, a single-helix phase mask in the emission path and postprocessing using multiview image fusion. The microscope implementation demonstrated here allows for postacquisition refocusing within a range of about 3.5 wavelengths while improving detection efficiency and sectioning quality compared to a confocal microscope due to the nonlinear signal generation.

Funding. National Science Foundation (NSF) (1429782, 1548924, 1556473); Austrian Science Fund (FWF) (P30214-N36); Small Business Innovation Research (SBIR) Program (1353638, 1534745).

Disclosure. R. P. has a financial interest in Double Helix LLC, which, however, did not support this work.

REFERENCES

1. W. Denk, J. H. Strickler, and W. W. Webb, Science **248**, 73 (1990).
2. F. Helmchen and W. Denk, Nat. Methods **2**, 932 (2005).
3. W.-F. Cheong, S. A. Prahl, and A. J. Welch, IEEE J. Quantum Electron. **26**, 2166 (1990).
4. M. Ingaramo, A. G. York, P. Wawrzusin, O. Milberg, A. Hong, R. Weigert, H. Shroff, and G. H. Patterson, Proc. Natl. Acad. Sci. USA **111**, 5254 (2014).
5. P. W. Winter, A. G. York, D. Dalle Nogare, M. Ingaramo, R. Christensen, A. Chitnis, G. H. Patterson, and H. Shroff, Optica **1**, 181 (2014).
6. I. Gregor, M. Spiecker, R. Petrovsky, J. Großhans, R. Ros, and J. Enderlein, Nat. Methods **14**, 1087 (2017).
7. C. J. Sheppard, M. Castello, G. Tortarolo, G. Vicidomini, and A. Diaspro, J. Opt. Soc. Am. A **34**, 1339 (2017).
8. C. J. Sheppard, Optik **80**, 53 (1988).
9. C. B. Müller and J. Enderlein, Phys. Rev. Lett. **104**, 198101 (2010).
10. M. Ingaramo, A. G. York, E. Hoogendoorn, M. Postma, H. Shroff, and G. H. Patterson, Chem. Phys. Chem. **15**, 794 (2014).
11. C. Roider, R. Heintzmann, R. Piestun, and A. Jesacher, Opt. Express **24**, 15456 (2016).
12. A. Jesacher, M. Ritsch-Marte, and R. Piestun, Optica **2**, 210 (2015).
13. C. Roider, R. Piestun, and A. Jesacher, Optica **4**, 1373 (2017).
14. F. Strasser, M. Offterdinger, R. Piestun, and A. Jesacher, are preparing a manuscript to be called "Spectral image scanning microscopy."
15. R. Di Leonardo, F. Ianni, and G. Ruocco, Opt. Express **15**, 1913 (2007).
16. R. Piestun and S. A. Quirin, "Methods and systems for three dimensional optical imaging, sensing, particle localization and manipulation," U.S. patent 14031887, September 19, (2013).
17. M. D. Lew, S. F. Lee, M. Badieirostami, and W. Moerner, Opt. Lett. **36**, 202 (2011).
18. S. Prasad, Opt. Lett. **38**, 585 (2013).
19. C. J. Sheppard, S. B. Mehta, and R. Heintzmann, Opt. Lett. **38**, 2889 (2013).